



Transtensional coseismic fault slip of the 2021 Mw 6.7 Turt Earthquake and heterogeneous tectonic stress surrounding the Hovsgol Basin, Northwest Mongolia

Xiaoge Liu ^a, Wenbin Xu ^{a,*}, Natalia A. Radziminovich ^b, Nan Fang ^a, Lei Xie ^c

^a School of Geosciences and Info-Physics, Central South University, Changsha 410083, Hunan, PR China

^b Institute of the Earth's Crust, Siberian Branch of the Russian Academy of Sciences, Lermontov Str., 128, Irkutsk 664033, Russia

^c The Department of Land Surveying and Geo-Informatics, The Hong Kong Polytechnic University, Hong Kong, China

ARTICLE INFO

Keywords:

Coseismic InSAR displacement
Transtensional slip distribution
Tectonic stress heterogeneity
Half-graben
Coulomb stress change

ABSTRACT

Knowledge of the regional crustal deformation and stress field is fundamental to understanding and constrain the ongoing evolution of Hovsgol basin, northwest Mongolia. The 2021 Mw 6.7 Turt earthquake provides an unprecedented opportunity to probe the local tectonic stress field and upper crust deformation. We investigate the coseismic surface displacements and invert fault slip models using Interferometric Synthetic Aperture Radar observations and teleseismic data. The mainshock occurred as a result of normal faulting with a right-lateral strike-slip component on an NW striking plane, which is consistent with the transtensive local stress field inverted from regional focal mechanisms. It is surrounded by transpressive and strike-slip stress fields proposed by previous studies indicating regional stress heterogeneity probably controlled by the distinct structure geometries in and around Hovsgol basin. Our results also suggest that the current deformation of the Hovsgol basin is dominated by half-graben forming. Seven historical strong earthquakes (M 7) may advance the 2021 Turt earthquake by ~12% recurrence interval, based on the assumption of equal stress release from recurrence earthquakes, meanwhile, the 2021 Turt earthquake may increase the potential seismic hazard on the neighbor Mondy and South Hovsgol faults, which deserves more attention.

1. Introduction

The Hovsgol basin, northwest Mongolia is situated in the western closure of the Baikal rift system. This rift system is located within the Asian continent interior, and is one of the most active discrete rifts representing the early stages of continental split-up (Petit and Déverchère, 2006). GPS measurements suggest that ~15% of the India-Eurasia convergence (~40 mm/yr) is accommodated within the Baikal Rift System and Mongolia (Calais et al., 2003; Wang and Shen, 2020). The western part of the Baikal rift system is located within the Central Asian mobile belt which traces along the southern margin of the Siberian craton. This belt near the Siberian craton consists of a number of Precambrian and Early Paleozoic terranes (Gladkochub and Donskaya, 2009). The Cenozoic Hovsgol basin has been formed along the border of the Tuva-Mongolian Riphean microcontinent with the early Paleozoic Khamardaban block (Vasiliev et al., 1997). The basin is a graben with the steep western side bordered by the Hovsgol master fault. This

graben-forming stage is still continuing, which divides the Hovsgol Unit into west-Hovsgol dome-blocky uplift and the east-Hovsgol arch-like structure during the neotectonics stage (Gladkochub and Donskaya, 2009).

The considered area is a key region where compression due to the Indo-Eurasia collision meets extension due to Baikal rifting. In the northern Mongolia, three narrow basins, oriented S–N, namely the Busingol, the Darkhad, and the Hovsgol basins, are supposed to be rift basins; however, the recent stress field here has been evaluated as transpression (San'kov et al., 2011). Reconstructed on tectonic fracturing, slickenside in outcrops of dated Cenozoic formations and basement rocks, the stress field of the Hovsgol basin shows temporal changes from extension in NW-SE direction in Miocene to compression in this direction for a short time in Late Pliocene, and then at the latest stage (Quaternary) to strike-slip and transpression stress field with orientations of NE-SW compression axis and NW-SE tension axis (San'kov et al., 2004). Other studies show that the present-day stress field in the region

* Corresponding author.

E-mail address: wenbin.xu@csu.edu.cn (W. Xu).

is defined as compressional stress regime (Arjannikova et al., 2004; Melnikova et al., 2004; Ritz et al., 2000). However, there is no consensus on the type of stress regime in Hovsgol basin. Combined seismological focal mechanisms and geological observations, Delouis et al. (2002) provide the stress inversion results indicating the Hovsgol basin is under pure extensive stress regime, while wrench-extensional regime is also proposed for the Hovsgol basin (Khilko et al., 1985; Misharina et al., 1983; Petit et al., 1996; Radziminovich et al., 2016). In addition, the seismic focal mechanism solutions of the 2021 Hovsgol mainshock from several organizations showed a consistent normal faulting (Fig. 1b). However, their magnitude of strike slip component and focal depth (10–20 km) is inconsistent (Table 1). These discrepancies indicate that the regional tectonic stress is rather complicated.

On 11 January 2021, an Mw 6.7 earthquake occurred in the northern part of the Hovsgol basin. It is the largest instrumentally recorded event here, providing an opportunity for studying the stress heterogeneity in the region. However, only a few geodetic studies were carried out with limited campaign GPS sites (Bayasgalan et al., 2005; Calais et al., 2003; Vergnolle et al., 2003), which are not located in the coseismic region. Fortunately, space geodetic Interferometric Synthetic Aperture Radar (InSAR) technology captures the coseismic surface displacement caused by the 2021 Turt earthquake. This permits us to study the crust deformation and stress regime in the Hovsgol basin. After the earthquake, few papers have been published. Combining seismological and InSAR observations, Liu et al. (2021) found the rupture kinematics of this earthquake propagates toward northwest with average rupture velocity of ~2.0 km/s and complex oblique slip with average rake angle of 140°. Bayaraa et al. (2021) investigated the epicenter region in the field five days after the earthquake and found some 100-m-scale surface cracks

but without primary coseismic rupture. However, these studies rarely analyze the associated stress characteristics based on the earthquake, which are important for understanding the regional basin evolution and seismic hazard. Here, we use Sentinel-1 Synthetic Aperture Radar (SAR) images to map the coseismic InSAR displacements following the 2021 Turt Mw 6.7 earthquake. Combining the teleseismic P-wave data, we jointly constrain the seismogenic fault geometry and finite slip model. Using the previous data on earthquake focal mechanisms, we make stress inversion to reveal how the displacement of the Turt earthquake relates to the stress field. Finally, we analyze seismic risk in the Hovsgol region by estimating the Coulomb stress change after the Turt earthquake.

2. Data processing and inversion methods

2.1. Coseismic data processing

2.1.1. InSAR data

The Turt earthquake occurred in the remote northwestern of Mongolia, where few ground-based geodetic observations (i.e., GPS) are available near the epicenter (Calais et al., 2003; Wang and Shen, 2020). However, the favorable conditions of arid climate and low erosion rates (Meltzer et al., 2019) permit us to employ InSAR technology to obtain the space geodetic displacements for this earthquake even with the C-band SAR images. SAR data acquired by the Sentinel-1 satellite provide a unique opportunity to quantify surface displacements of the Turt earthquake and to constrain the activated normal fault structures beneath the Lake Hovsgol (Fig. 1). Using the Gamma software (Wegmüller et al., 2016), high-accuracy coregistration of the primary and

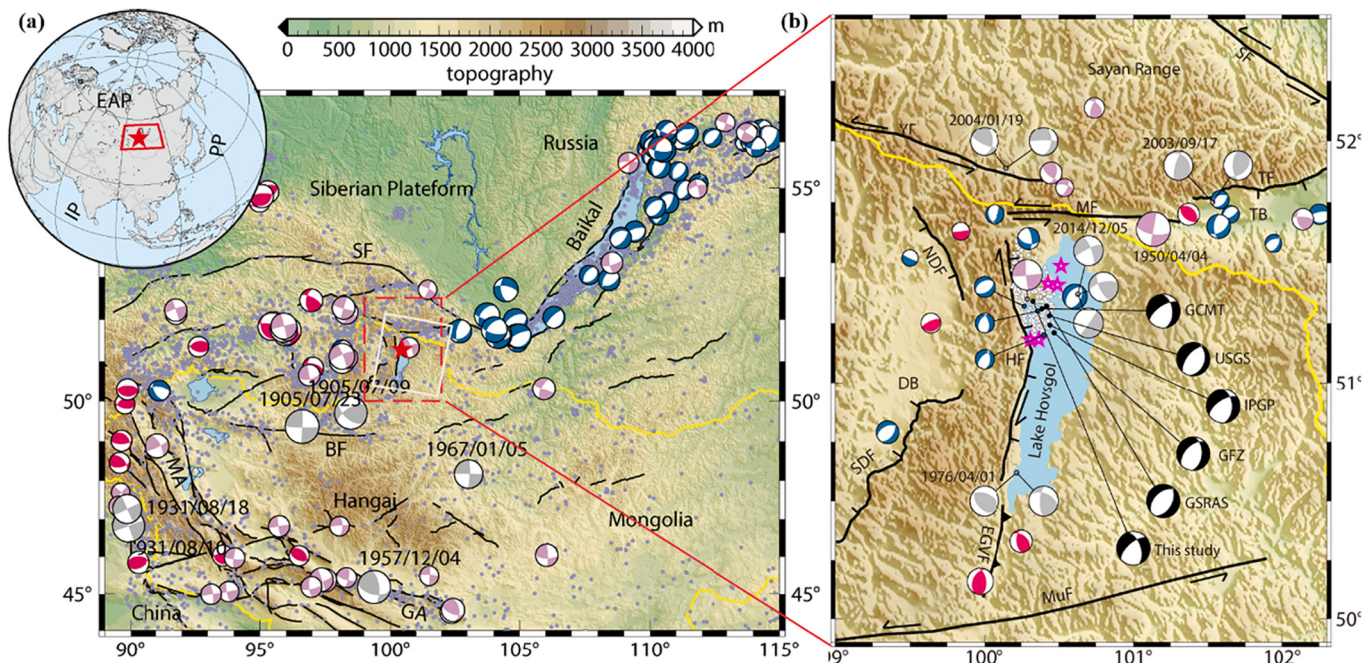


Fig. 1. Regional seismotectonic context around the 2021 Turt, Mongolia earthquake. (a) Red star represents the epicenter of the mainshock from USGS. Blue, pink and red focal mechanisms represent normal-, strike-slip, and thrust-dominated events from International Seismological Centre (ISC, <http://www.isc.ac.uk/iscbulletin/search/fmechanisms/interactive/>), respectively. Gray moment tensors are historical great earthquakes with $M > 7$. Purple dots are epicenters for earthquakes since 1900. Black lines are the main active faults from GEM Global Active Faults (<https://github.com/GEMScienceTools/gem-global-active-faults>). White rectangles represent the spatial extent of Sentinel-1 SAR data from one descending track (DT4). Yellow line shows the border between China, Mongolia and Russia. Dashed red rectangle bounds the extent of enlarged Fig. 1b. The inset shows the location of the study area. IP, Indian Plate; PP, Pacific Plate; EAP, Eurasian Plate. (b) The detailed tectonic background in the study area. Black focal mechanisms represent solutions for the mainshock from different catalogs (Table 1). White dots are the aftershocks from the Baikal Branch of the Geophysical Survey of Russian Academy of Sciences, and purple stars are six $Mw > 5$ aftershocks from USGS. SF, Sayan Fault; BF, Bolnay Fault; TF, Tunka Fault; MF, Mondy Fault; YF, Yamaatinskii Fault; HF, Hovsgol Fault; NDF, North Darkhat Fault; SDF, South Darkhat Fault; EGVF, Egiin-Gol Valley Fault; MuF, Murn Fault; MA, Mongolian Altay; GA, Gobi Altay; TB, Tunka Basin; DB, Darkhat Basin. Note that the south Hovsgol Fault and Murn Fault are compiled from previous studies and geomorphology (Jolivet et al., 2013; Petit et al., 2002; Ritz et al., 2018; Schlupp and Cisternas, 2007). (For interpretation of the references to colour in this figure legend, the reader is referred to the web version of this article.)

Table 1

Source parameters for the 2021 Turt earthquake. USGS, U.S. Geological Survey (<https://earthquake.usgs.gov>); GCMT, Global Centroid-Moment Tensor Project (<https://www.globalcmt.org/>); GFZ, GeoForschungsZentrum (GEOFON) Moment Tensor Solutions (<http://geofon.gfz-potsdam.de/eqinfo/>); IPGP, Institute de Physique du Globe de Paris (<http://www.ipgp.fr/fr>); GSRAS, Geophysical Survey of Russian Academy of Sciences (http://www.ceme.gsras.ru/new/ssd_news.htm).

Source	Lon (°)	Lat (°)	Depth (km)	Strike (°)	Dip (°)	Rake (°)	Mw
USGS	100.438	51.281	11.5	16/219	32/60	-110/-78	6.74
GCMT	100.39	51.31	14.3	354/236	45/65	-143/-52	6.8
GFZ	100.47	51.21	18	4/226	47/51	-121/-60	6.7
IPGP	100.443	51.241	13	358/237	46/62	-139/-52	6.84
GSRAS	100.42	51.32	20	29/228	46/46	-103/0	Mb 6.5
Liu et al. (2021)	100.437	51.277	11	345	42	140 ^a	6.75
This study	100.33 ^{+0.01} _{-0.01}	51.34 ^{+0.01} _{-0.02}	8.9 ^{+0.6} _{-0.2}	340.4 ^{+1.0} _{-1.6}	53.9 ^{+7.0} _{-4.0}	-146.4 ^{+4.6} _{-5.8}	6.75 ^{+0.13} _{-0.17}

^a Positive rake angle in the study of Liu et al. (2021) is attributed to different geometric definitions (i.e., 90° rake angle represents normal slip but dip slip in our definition), but with same meaning of normal slip and right-lateral strike slip in our study.

secondary Single Look Complex (SLC) products from descending tracks were firstly carried out (Table S2). Then, we constructed coseismic interferograms with the coregistered primary and secondary SLCs. After removing the effect of topography with the 30 m Shuttle Radar Topography Mission digital elevation model (Farr et al., 2007), an improved power spectrum filter method was applied to minimize the phase noise in the interferograms (Li et al., 2008). We unwrapped the filtered pairs of interferograms by a minimum cost flow method (Chen and Zebker, 2001), and geocoded the unwrapped interferograms to obtain the coseismic surface displacement fields. Considering the substantial topographic relief surrounding the Lake Hovsgol, possible topography-dependent tropospheric delay was estimated and removed (Xu et al., 2017).

2.1.2. Teleseismic data

In addition to InSAR data, we also collected P wave records from 43 teleseismic stations at epicentral distances between 30° and 90° (Fig. S1) compiled by the Incorporated Research Institutions for Seismology (IRIS). The initial P wave records were firstly processed to minimize the influence of instrument response (Wald et al., 1996), and then a band-pass filter (0.01–0.5 Hz) was applied to suppress the noises. In addition, the teleseismic stations in the southern azimuth were excluded due to the low signal-to-noise ratio. Time window of waveforms was tapered as 98 s with 30 s before the initial arrivals (Figs. 2 and S2). The global velocity model AK135 is used for teleseismic Green's function calculation.

2.2. Fault geometry and distributed slip inversion

Before performing inversions for the Turt earthquake fault geometry, we first downsampled the InSAR interferograms with a quadtree algorithm (Jónsson et al., 2002) to a computationally tractable size. Covariances of the downsampled data are estimated with the variability of raw observations within the downsampled grids and employed to weight the observations in the following inversions. In order to provide extra constrain on the fault geometry, P wave records data from IRIS and GEOFON are also introduced. The variances of P-wave data are estimated based on the data fluctuation before the P-wave arrival time. Bayesian Earthquake Analysis Tool (BEAT) is applied to determine the fault geometry parameters and their uncertainties (Vasyura-Bathke et al., 2020). To broadly cover the solution space and better quantify the associated uncertainties, a relatively loose sampling boundary is set up for fault geometry parameters according to prior knowledge (e.g., focal mechanisms from USGS/GCMT/GFZ/IPGP/GSRAS etc.) (Table 1 and Table S3). More detailed information about the nonlinear inversion can be found in (Vasyura-Bathke et al., 2020).

To resolve a distributed slip coseismic model fitting the observations better, we fixed the fault geometry derived from joint InSAR and teleseismic data inversion and extended the fault size with length of 50 km and width of 30 km (24 km in depth), and the fault was divided into $2 \times$

2 km subfaults. Being more finely discretized, sources are generally overparameterized, which commonly requires smoothness constraints to stabilize the solutions (Jónsson et al., 2002; Xu, 2017). Considering the well distributed coseismic slip inversion with both InSAR and seismic data by Liu et al. (2021), InSAR data only are used in our distributed slip inversion to improve computational efficiency. We used the Laplacian regularization with smoothing factor determined from Cholesky decomposition of off-diagonal terms in a Gaussian prior $p(s|\beta)$. The maximum-a-posterior solution for strike, dip, and slip (e.g., rake-perpendicular and rake-parallel slip components) and the Laplacian smoothing factor β is obtained with sequential Monte Carlo method (Del Moral et al., 2006). During the distributed coseismic slip inversion, the range of rake-perpendicular and rake-parallel slip components are constrained as [-1,1] and [0,2], respectively, based on the slip magnitude of our uniform slip inversion and previous study (Liu et al., 2021). More detailed information can be found in (Vasyura-Bathke et al., 2020).

2.3. Focal mechanism data and stress inversion

We estimate the stress field from the focal mechanism solutions of the Hovsgol region which come mainly from regional solutions published in the regular catalogs and some papers. The dataset includes focal solutions for 27 earthquakes that occurred before the 2021 Turt event (Table S1, Fig. 6). The vast majority of mechanisms were determined by the method of first motion polarity of P waves at the regional stations. Four earthquakes have several solutions obtained by different authors (Fig. 1b). The strongest earthquake in the area is the 1950 Mw6.9 Mondy earthquake occurred at the western termination of the Tunka basins.

There are several methods for determining tectonic stress from focal mechanisms. The most commonly used methods have been developed by (Gephart and Forsyth, 1984; Michael, 1984; Michael, 1987), which have been expanded and modified by (Lund and Slunga, 1999; Martínez-Garzón et al., 2016; Vavryčuk, 2014). An iterative joint inversion method (Vavryčuk, 2014) was adopted to calculate principal stresses σ_1 , σ_2 , σ_3 with $\sigma_1 > \sigma_2 > \sigma_3$ under the positive compression stress convention, and the stress ratio $R = (\sigma_1 - \sigma_2)/(\sigma_1 - \sigma_3)$, $0 < R < 1$ describing the relative magnitudes of the principal compressive stresses (Warren-Smith et al., 2019). This method is suitable for regions even without information about actual tectonic faults. This is attributed to a fault instability algorithm identifying a more likely nodal plane (Lund and Slunga, 1999; Vavryčuk et al., 2013), which has little influence on the accuracy of stress field orientations but significant improvement on the stress ratio. Additionally, this method allows one to quantify the confidence intervals of optimal stress tensor by bootstrap resampling approach (Michael, 1987), in which each nodal plane can be selected with equal probability during the sampling.

For stress inversion, we used the focal mechanisms of earthquakes which occurred before the Turt earthquake (Table S1, Fig. 5) and the

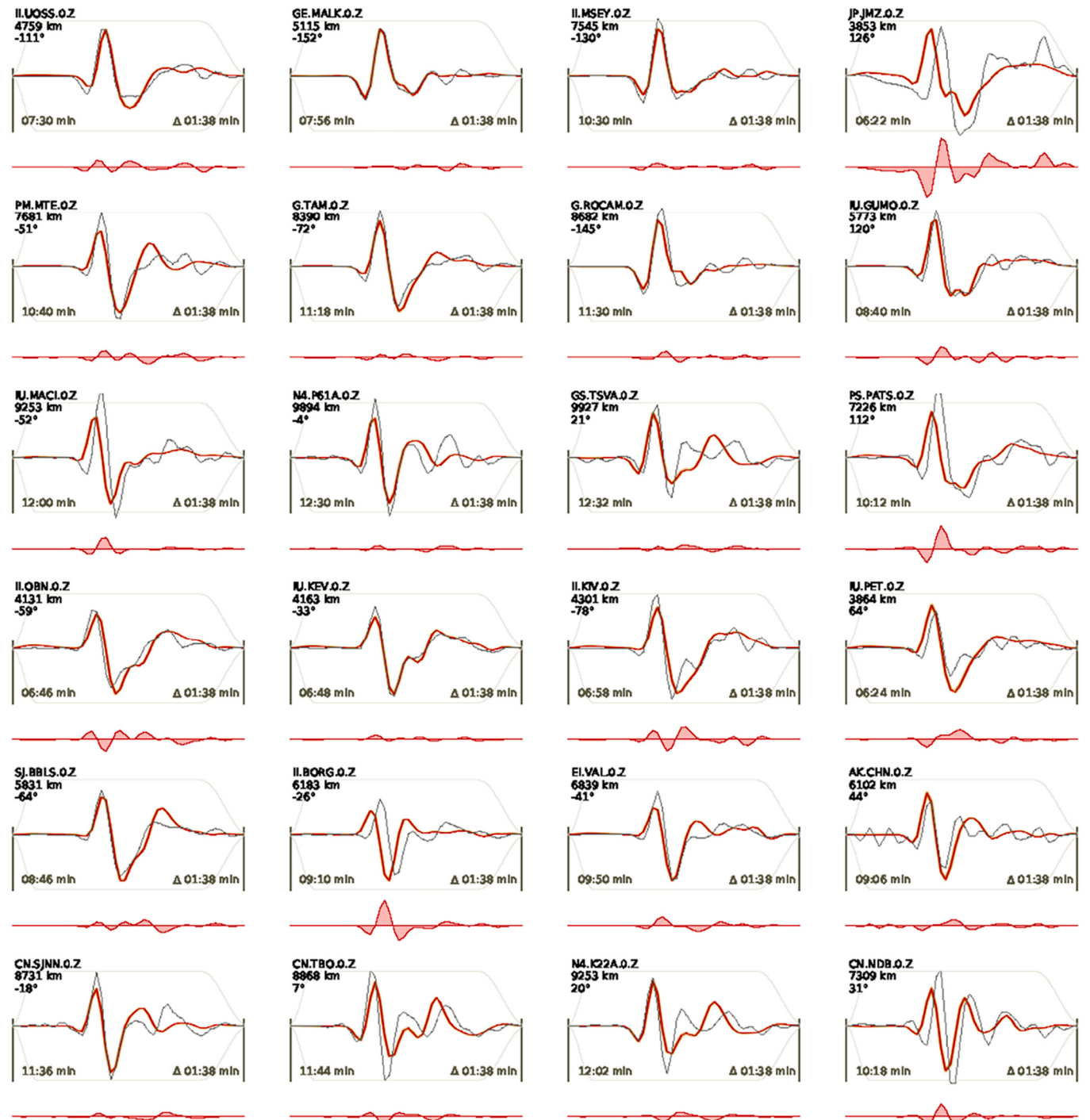


Fig. 2. Comparison between the observed teleseismic P waves and the synthetic waveforms obtained from the joint inversion of uniform fault slip model. The filtered (0.01–0.1 Hz) displacement waveform data (gray line) and the filtered synthetic displacement waveforms (red line) are shown together. Brown shading indicates 100 random draws of the filtered synthetic waveform displacements from the posterior probability density. Red-line polygons below each waveform subplot represent the residual waveforms. Each subplot is annotated with the station name, component, the distance, and azimuth angle from the maximum a-posteriori solution from the center of the reference fault. The arrival time and the duration of each station are shown in the lower left and right, respectively. (For interpretation of the references to colour in this figure legend, the reader is referred to the web version of this article.)

mainshock (our solution) (Table 1 and Table S1). Two samples were taken: the total sample given in Tables and only for the northern part of the Hovsgol area. We estimated 2000 bootstrap samples with random noise 10° to obtain 95% confidence region of optimal stress tensor. The average misfit angle α between the observed and predicted fault slip directions can be used to evaluate the success of stress inversion.

3. Results

3.1. Coseismic InSAR displacement of the 2021 Turt earthquake

The excellent coherence and generally low noise level in the coseismic interferogram characterize well-defined surface displacements associated with the Turt earthquake (Fig. 3). The displacements

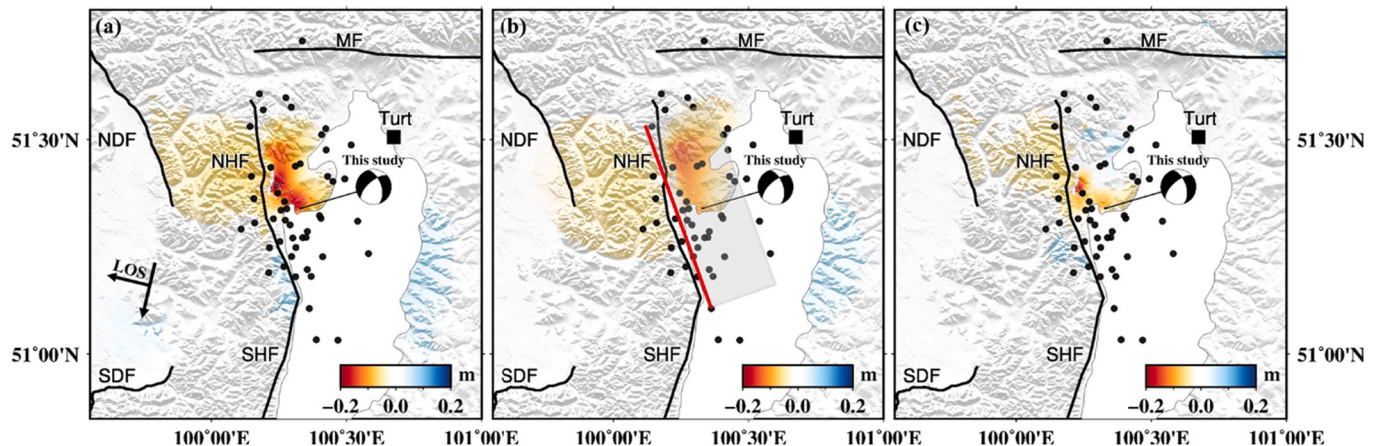


Fig. 3. Observed and modeled coseismic ground displacements in satellite line of sight (LOS) direction. (a) the observed ground deformation fields; (b) model predictions; (c) residuals between observations and models. Black moment tensor and dots represent USGS solution and aftershocks. The shade box in (b) represents the ground projection of the seismogenic fault with the red solid line indicating the fault trace. The fault abbreviations are identical to those in Fig. 1. NHF, north Hovsgol Fault; SHF, south Hovsgol Fault. (For interpretation of the references to colour in this figure legend, the reader is referred to the web version of this article.)

are mainly distributed between the north Hovsgol Fault (Fig. 3) and west bank of Lake Hovsgol. Little coseismic displacement can be observed on the neighboring NNE-SSW striking south Hovsgol Fault, which may inhibit propagation of coseismic rupture (Wilson et al., 2009). The descending coseismic displacement field shows obvious up to ~20 cm surface subsidence away from the satellite line of sight (LOS) direction, indicating the significant displacement zone is located at the hanging wall of the normal fault. There is no obvious range decrease in the radar LOS direction except for the about ~5 cm LOS uplift along the east bank of Lake Hovsgol (Fig. 3a). It is worthy to note that coseismic

interferogram covers six Mw 5 and other aftershocks, which occurred on the same day of the mainshock. In addition, the descending coseismic displacement contains more than one day of other postseismic transients. These indicate that the coseismic displacements may be affected, to some extent, by postseismic activities (Liu and Xu, 2019; Lu and Zhou, 2021; Tang and Sun, 2021).

3.2. Fault geometry and slip distribution

There are several fault-plane solutions for the Turt earthquake issued

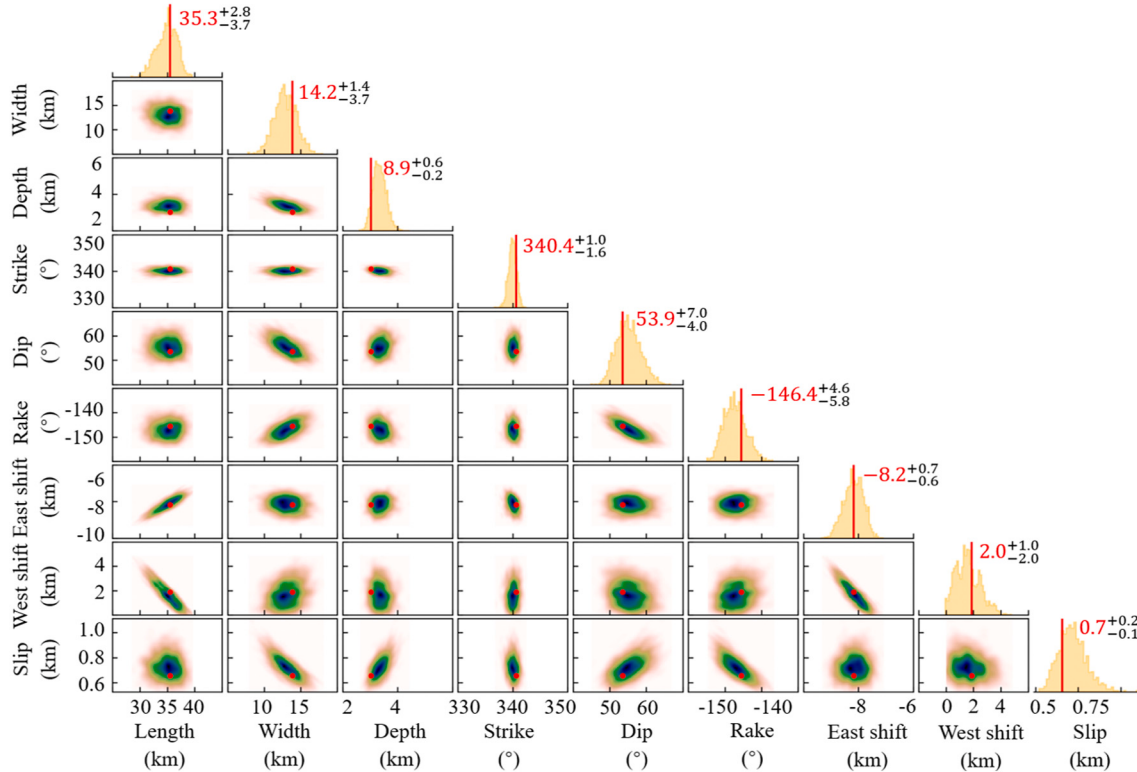


Fig. 4. Posterior probability distributions for the fault model parameters of the 2021 Hovsgol earthquake. Red lines and cycles represent the maximum-a-posteriori probability solution. Scatter plots are contoured according to frequency (cold colors for high frequency, warm colors for low frequency). The optimal parameters and their uncertainties are labeled next to the histograms. (For interpretation of the references to colour in this figure legend, the reader is referred to the web version of this article.)

by different seismological agencies (Table 1). After the complete solution search for strike [0°, 360°], dip [0°, 90°], and rake [-180°, 180°] angles (Table S3), our results of nonlinear inversion show that the optimal fault plane was the NNW-SSE oriented plane (Table 1, Table S3). This confirms that the north Hovsgol Fault is the seismogenic fault nucleating the 2021 Turt earthquake. The maximum posterior probability uniform slip model solution obtained after 10⁶ iterations with sequential Monte Carlo method, raising the preferred fault plane of 35 km long and 14 km wide with a strike angle of 341°, a dip angle of 54°, and a rake angle of -146° (Table 1). This is consistent with the field-mapped fault trace along the west side of Lake Hovsgol (Fig. 1) and explains well the observed P waveform data (Fig. 2). Trade-offs between the fault parameters are not obvious (i.e., strike, dip and rake angles) as shown in the histograms of posterior probability distributions (Fig. 4).

The optimal distributed coseismic slip inversion results indicate that the 2021 Turt earthquake ruptured on a fault structure with a length of ~35 km (coseismic slip >0.2 m) along the west bank of Lake Hovsgol (Fig. 5), which successfully reproduces the InSAR observations (Fig. 3). The similar rake directions of the distributed coseismic slip can be attributed to the smaller rake-perpendicular slip component than the rake-parallel slip component. The RMS of observations and model predictions are about 2 cm for InSAR observations. The coseismic slip is mainly concentrated at depths of 2–10 km with a peak slip of 1.2 m located at 7 km depth. The uncertainty of slip on each patch is marked by ellipses in Fig. 5. The near-field residuals may be resulted from the combined contributions of residual atmospheric artifacts, early unmodeled postseismic deformation (e.g., afterslip or poroelastic rebound), non-planar fault geometry, multi-segments faulting along strike and inelastic deformation. Assuming the average shear moduli is 34 GPa in the Hovsgol region (Laske et al., 2013), we calculated a geodetic moment (M_0) as ~2.46 × 10¹⁹ Nm. The estimated geodetic moment is corresponding to M_w 6.75, which is generally consistent with different catalogs (Table 1). Interestingly, the finite coseismic fault slip reveals that the slip is characterized by comparable dip-slip and right-lateral slip component (rake = -146°), which is comparable to the previous study (Liu et al., 2021). In addition, no obvious shallow (0–2 km in depth) coseismic slip may indicate the shallow slip deficit (Fialko et al., 2005; Xu et al., 2019), which is consistent with no primary surface coseismic rupture in the field study (Bayaraa et al., 2021).

3.3. Stress inversion

The achieved stress inversion results are reported and summarized in Fig. 6 and Table 2, showing the stress fields in and around the Hovsgol basin is rather complicated. The sub-horizontal σ_1 axes in North Hovsgol Region (NHR) with NE-SW orientation and a low R (0.43) value indicating slightly difference in magnitude between σ_1 and σ_2 (Fig. 6b), coupled with horizontal σ_3 (Table 2), implies the NHR is under coexistence of both normal and strike slip stress regimes. The NHR is characterized by well-defined 95% confidence regions of sub-horizontal principal stress σ_3 . In addition, we inverted all the compiled focal mechanisms for average stress filled in and around Hovsgol basin (Fig. 6a and c). It is similar to the stress filed of NHR but with smaller plunge angle (45°) of σ_1 axes, indicating the more strike-slip component in the total region. The much larger average misfit angle 57° in the total study region than that 29° in the NHR (Fig. S3 and Table 2), indicating the background tectonics stress fields in and around Hovsgol basin are highly heterogenous assuming all the compiled solutions within acceptable uncertainties (Michael, 1991). According to the method of Lund and Townend (2007), we estimated the direction of the maximum horizontal stress (SHmax) from the inverted three principal stresses and stress ratio (Pan et al., 2020). The SHmax are 032° and 052° for the NHR and the total region, respectively (Table 2).

According to the scheme of stress regime characterization and maximum horizontal compressive stress orientation (SHmax) proposed by (Zoback, 1992) based on the plunge and azimuth angles of stress axes, the results show that it is under extensional and transtensional stress fields for the NHR and the entire study region, respectively. However, our inverted plunge angle (59°) of maximum principal stress in the NHR is close to the critical plunge angle (52°, NF for σ_1 , $\text{plunge} > 52^\circ$ and σ_3 , $\text{plunge} < 35^\circ$, NS for $40^\circ < \sigma_1$, $\text{plunge} < 52^\circ$ and σ_3 , $\text{plunge} < 35^\circ$) according the categories of Zoback (1992). This indicates the stress regime in Hovsgol Basin is not pure extensional but with a significant strike-faulting mechanism, which is consistent with the transtensional coseismic slip (Liu et al., 2021; this study). The typical girdle distributions of σ_1/σ_2 and small stress ratio indicate a possible stress permutation between σ_1 and σ_2 (Fig. 6) (Hu and Angelier, 2004). This switches between σ_1 and σ_2 are expressed by close association between normal and strike slip faulting (Hu and Angelier, 2004), which is consistent with faulting

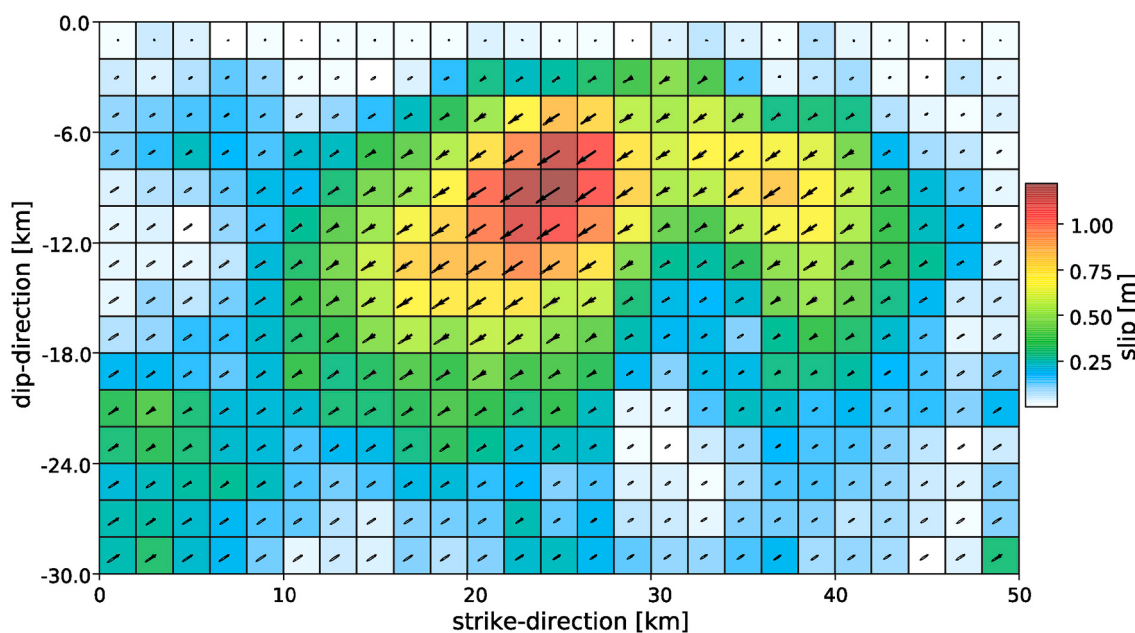


Fig. 5. Coseismic slip distribution solution for the 2021 Turt earthquake estimated using InSAR interferogram. The colour patches and black arrows show the value and direction of the maximum-a-posterior solution. The two-sigma confidence interval is indicated by black ellipses around the arrow tips.

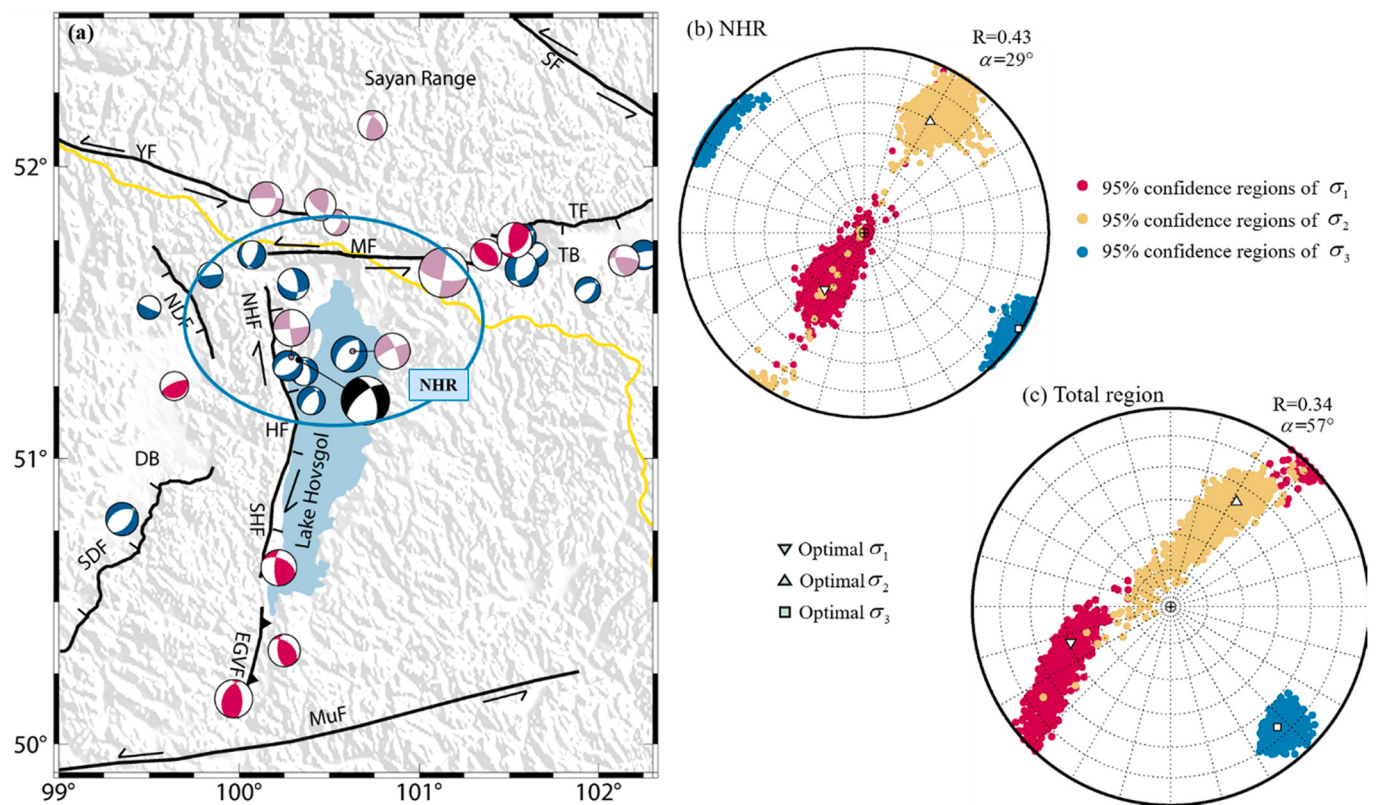


Fig. 6. The stress tensor inversion. (a) Focal mechanisms in the lower hemisphere projection used in the stress inversion for the entire region and for the northern part of the Hovsgol basin; (b) results of stress inversion for the northern part of the Hovsgol area; (c) results of stress inversion for the entire region.

Table 2

Stress tensor parameters as obtained from focal mechanisms inversion.

Subregions	N ^a	$\sigma_1(^{\circ})$ az./pl. ^b	$\sigma_2(^{\circ})$ az./pl.	$\sigma_3(^{\circ})$ az./pl.	R ^c	$\alpha(^{\circ})$ ^d	Stress Regime	SHmax ^e
North Hovsgol	12	215/59	031/30	122/2	0.43	29	NF	032
Total region	29	250/45	032/38	138/20	0.34	57	NS	052

^a Number of focal mechanisms.

^b Azimuth and plunge angles.

^c Stress ratio $R = (\sigma_1 - \sigma_2)/(\sigma_1 - \sigma_3)$, $0 < R < 1$.

^d Misfit angle.

^e Maximum horizontal compressive stress orientation.

behavior of the north Hovsgol region, dominated by steep (plunge angles 59°) dip NE-SW compression inducing normal faulting with strike-slip component (Fig. 6 and Table 2).

4. Discussion

4.1. Faulting and stress heterogeneity in the Hovsgol basin region

The 2021 Mw 6.7 Turt earthquake is the largest instrumentally recorded event occurred within the Hovsgol basin. It is supposed to be caused by movement on the NW striking plane resulting from normal faulting with a right-lateral strike-slip component (Liu et al., 2021; this study). The solution obtained in our study is in agreement with tensor moments issued by GCMT and IPGP, while other available solutions show mostly normal faulting (Fig. 1b and Table 1). The type of displacement in our focal mechanism corresponds to the kinematics of the NW fault determined from geological-structural data (San'kov et al., 2004). The field data described in (San'kov et al., 2004) also show, along with facets characterizing normal fault movements, regular right-lateral shear displacements of high-order stream valleys and asymmetric fanning cones. The stress regime deduced from the mainshock and previous

focal mechanisms is transtension (Table 2), which is consistent with the oblique slip containing both normal- and dextral-slip (Liu et al., 2021; This study); while earlier it was defined as pure extensive (Delouis et al., 2002). Since the stress inversion results are highly dependent on the input events, we argue that the more complete catalog for the Hovsgol basin in our study than previous studies (e.g., Delouis et al., 2002; Melnikova et al., 2004; Radziminovich et al., 2016; San'kov et al., 2004) provide a more compelling evidence. Thus, we suggest that the northern part of the Hovsgol basin is under extensional conditions with a right strike-slip component on NW oriented faults. This extension seems to be local because it is surrounded by transpression and strike-slip stress regimes (Delouis et al., 2002; Melnikova et al., 2004; Radziminovich et al., 2016; San'kov et al., 2004). Spatially, the present-day stress field in the region is changing from compression in the southern part of the Hovsgol basin to extension in its northern part, and then, to the north of the Hovsgol basin, the stress field is transpressive (Delouis et al., 2002; Melnikova et al., 2004; Radziminovich et al., 2016; San'kov et al., 2004). This complex spatial stress regime transition is probably responsible for the large average misfit angle in the stress inversion for the entire considered region (Fig. 6, Table 2).

This indicates the complicated stress heterogeneity within the

Hovsgol region, which can be deduced from the stress inversion results in and around the Hovsgol basin (Fig. 6). It is also visible from the basin morphology which shows a widespread deforming zone in the north but relatively narrow rift in the south (Fig. 7). Specifically, the topography is relatively lower in the southern counterpart. Gravity data also indicates remarkable sedimentary thickness difference between north and south of the Hovsgol depression, with the maximum 550 m of sediments confined to the northern part of the depression, while the thickness of sediments rarely exceeds 350 m in the southern part of the Lake Hovsgol (Gladkochub and Donskaya, 2009; Zorin et al., 1989).

Reasons for heterogeneity of the tectonic stress are still under discussion (e.g., Hu and Angelier, 2004; Petit et al., 1996; Wileveau et al., 2007; Wilson et al., 2009; Barbot et al., 2009; Yale, 2003). The local extension, for example, was modeled as opening of the northern basin which is in a T-shape conjunction of the Mondy fault and Hovsgol fault, and the diagonal NW fault forms the block structure of this area (San'kov et al., 2004). After the Turt earthquake, most of aftershocks (~60,000 in the first three months) from local seismic stations, are located in the conjugate angle region between near E-W striking Mondy Fault and NW-SE north Hovsgol Fault, confirming activity of this block of the crust. In addition, stress heterogeneity including stress orientations and concentrations is attributed to active fault structures (Petit et al., 1996; Wilson et al., 2009; Yale, 2003), contrasting rheology (Hu and Angelier, 2004; Wileveau et al., 2007) and spatial variations of elastic properties (i.e., elastic moduli) (Barbot et al., 2009). Petit et al. (1996) suggest that inherited structures have a crucial influence on the local stress field changes within the Baikal rift zone, so that changes in stresses are spatially confined to changes in the Siberian craton boundary. The sudden fault strike changes from near E-W direction (Yamaatinskij Fault, Mondy Fault and TF) to near N-S direction (Hovsgol Fault, North Darkhat Fault and South Darkhat Fault), and then to NEE-SWW (Murn Fault) orientation is observed in the Hovsgol region (Fig. 1b, Fig. 7), which may geometrically control the stress heterogeneity from north to south here. This kind of influence of structure variations on stress field has also been proposed by 3-D distinct element modeling (Hu and Angelier, 2004) and observed in the Rotokawa Geothermal Field, New Zealand (McNamara et al., 2015).

Fault strike change is observed also along the western side of the

Hovsgol basin, from south Hovsgol Fault (010°) to north Hovsgol Fault (341°). According to some studies (Nicol et al., 2005; Wilson et al., 2009), the fault linkage point may control the displacements on the faults, so this change along the Hovsgol fault may inhibit the rupture propagation to south Hovsgol Fault, confirming by the coseismic displacement mainly confined surrounding north Hovsgol Fault during the Turt earthquake (Fig. 3). In this regard, it should be noted that seismicity of the instrumental period is concentrated in the northern part and southern tip of the Lake Hovsgol, while the south-central part of the lake (50.5° N - 51° N) seems to be a seismic gap where few earthquakes have been recorded (Dugarmaa et al., 2002; Radziminovich et al., 2016) (Fig. 1).

4.2. Half-graben-dominated depression

Hovsgol basin is generally considered as the result of subsidence on the down-dropped block of half-graben with the master steep western Hovsgol Fault hosting the 2021 mainshock. Some studies propose that only the western Hovsgol Fault is active, as it is clearly expressed in topography and geomorphology (Ivanov et al., 2015; Pollitz et al., 2003; Ritz et al., 2018). Some others, however, show the eastern minor Hovsgol fault (Petit et al., 1996; Tapponnier and Molnar, 1979; Wang et al., 2013). This makes it unclear whether Hovsgol basin is dominated by half- or full-graben. Our geodetic observations show a dominated subsidence observed on the western branch and no subsidence on the eastern branch (Fig. 3), indicating that the current subsidence is dominated by half-graben depression.

Lithology of the basin sides differs; Pliocene basalts are located on the eastern side of Hovsgol Fault, while it is relatively complex with sedimentary volcanic units (Riphean), Oselkovaya sedimentary series (Early Vendian) and Dzhidinsky sedimentary sequence (Middle Cambrian) on the western side (Fig. S4, <http://bic.iwlearn.org/en/atlas/atlas-of-the-baikal-basin-eng/view>). Bathymetry data of Lake Hovsgol indicates that the slope of the bottom of the lake is steep on the west and gentle on the east (Fig. 7), which is consistent with the observed fault scarps and steep slope on the west. This is also consistent with the west dome-blocky uplift and east arch-like structure features within Hovsgol basin (Gladkochub and Donskaya, 2009). Thus, the dominated

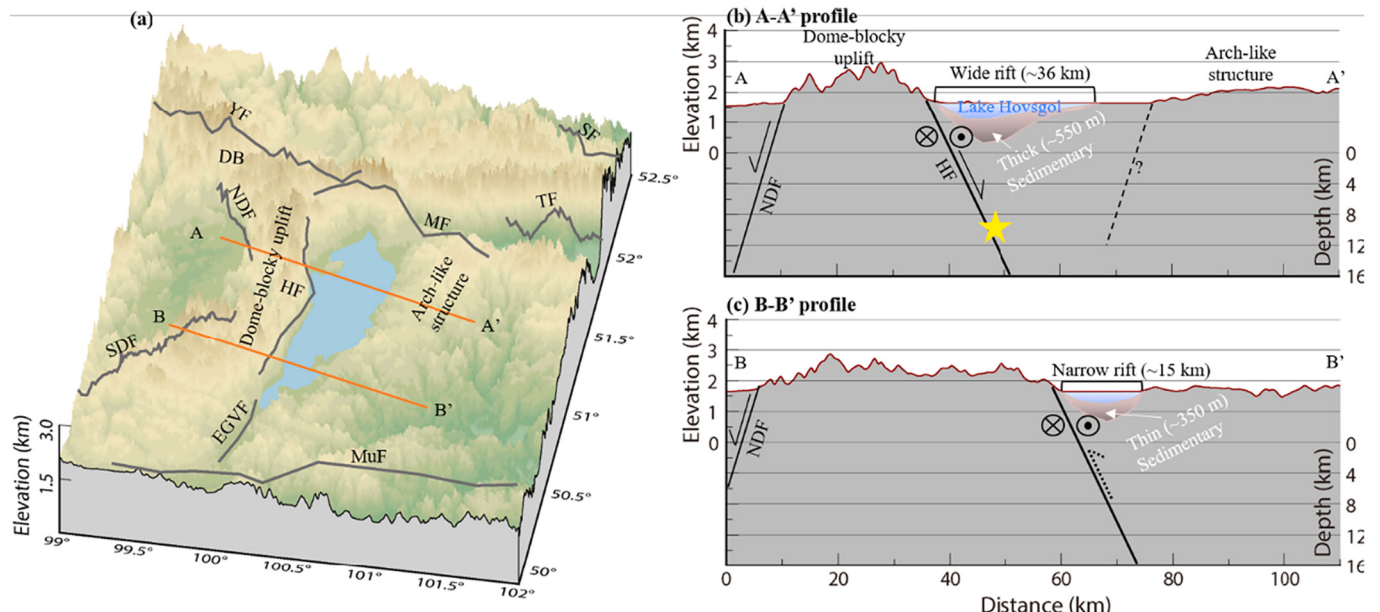


Fig. 7. Topography of the region. (a) The 3D view of topography in Fig. 1b. Gray lines represent active faults. The fault abbreviations are identical to those in Fig. 1. Orange lines are the two profiles shown in (b) and (c). (b) The 2D conceptional model on the profile A-A'. (c) The 2D conceptional model on the profile B-B'. Solid and dashed black lines represent the seismogenic fault and a possible oppositely dipping fault beneath the eastern bank of Lake Hovsgol. Yellow star indicates the hypocenter of the 2021 Turt earthquake. (For interpretation of the references to colour in this figure legend, the reader is referred to the web version of this article.)

west InSAR subsidence zone and remarkable difference of lithology, seismic activity, lake bathymetry, geomorphology fault scarps indicate that the current Hovsgol basin is still dominated by half-graben. Interestingly, coseismic InSAR observations also show surface displacement on eastern Lake Hovsgol bank (Fig. 3), implying the potential local structures. Aftershocks from local seismic stations show microearthquake ($M_L \sim 2$) cluster which agrees well with the displacement zone on eastern bank of Lake Hovsgol. These indicate that the minor structure may be activated by the 2021 Turt earthquake (Fig. 7b).

4.3. Regional seismic hazard

Considering the complicated heterogeneity stress background in the Hovsgol region, it is crucial to evaluate the influence of 2021 Turt earthquake on its surrounding active faults. Seismic stress triggering theory indicates that accumulated tectonic stress is suddenly released during earthquakes, the redistributed stress may influence the adjacent faults with stress triggers promoting the subsequent seismicity or stress shadows delaying the subsequent earthquake ruptures (Harris, 1998; King et al., 1994; Stein et al., 1994). Utilizing the coseismic slip model caused by the 2021 Turt earthquake as the driving source, and assuming the effective coefficient of $\mu = 0.4$, we estimated the static Coulomb Failure Stress changes (ΔCFS) triggered by the mainshock on the surrounding active faults (Lin and Stein, 2004; Toda et al., 2005).

The maximum positive and negative static ΔCFS both about 2.5 MPa are found on the north Hovsgol Fault (Fig. 8). The colour scale is logarithmic for a better visualization (Fig. 8). Strong stress triggers around coseismic rupture zone on north Hovsgol Fault may explain the aftershocks and indicates potential postseismic transients (e.g., afterslip, poroelastic rebound, and viscoelastic relaxation). This is consistent with the obvious postseismic deformation after the Turt earthquake, which is carrying out in another work (in preparation). Stress triggers (0.16 MPa, Fig. 8) are found on the west Mondy Fault, a sinistral strike slip fault dipping south which hosted the 1950 Mondy Mw 6.9 (Delouis et al., 2002). In addition, 0.03 MPa stress triggers are observed on the east tip of Yamaatinskiy Fault (Fig. 8 and Table S4); whereas the North Darkhat Fault, west Yamaatinskiy Fault and east Mondy Fault are mainly located in a stress shadow zone. It is obviously that the geometries of receiver faults play an important role in the ΔCFS calculations. For instance, the striking orientation changes significantly influence the polarity (stress triggers or stress shadows) of ΔCFS , which can be observed clearly on

fault North Darkhat Fault and South Darkhat Fault (Fig. 8). This kind of structure-orientation-related ΔCFS polarity is also reported, for example, in the case of 2020 Mw 6.5 Monte Cristo Range Earthquake (Zheng et al., 2020). This seems further confirming that the strikes change is one of the potential reasons for the stress heterogeneity in Hovsgol region. The calculated positive ΔCFS on the northward faults (east Yamaatinskiy Fault, west Mondy Fault, south Hovsgol Fault and central Murn Fault) exceeds the earthquake triggering threshold 0.01 MPa (Hardebeck et al., 1998). This indicates that the seismic hazard for these faults may be potentially increased, especially for the West Mondy Fault.

To further investigate the stress impact of historical large earthquakes surrounding the Hovsgol basin on the 2021 Turt earthquake seismogenic fault, we collect the source parameters of seven large earthquakes (M7, Fig. 1 and Table S5) to calculate the ΔCFS on Hovsgol Fault. Based on the collected focal mechanism of these seven large historical earthquakes and the same method above, the static ΔCFS triggered by these historical earthquakes are estimated on the Hovsgol Fault (Figs. 9). The collected source parameters of these historical earthquakes could contain significant uncertainties due to limited recorded observations (e.g., seismograms). Thus, it is valuable to improve the calculation of the ΔCFS if the refined source models are available (Yang et al., 2021). The results show that the polarities of the ΔCFS on the Hovsgol Fault are varied for different historical earthquakes (Fig. 9a-g), which seems to evidence again that structures geometry plays a significant role in local stress field. The calculated static ΔCFS are generally positive with an average value of 0.087 MPa on the north Hovsgol Fault (Fig. 9h). Although the negative ΔCFS ($\sim 10^{-3}$ MPa) on the north Hovsgol Fault are caused by the 1957 Gobi-Altai (Fig. 9f) and 1967 Mogod (Fig. 9g) earthquakes, which are much smaller than the positive ΔCFS (0.05–0.1 MPa) induced by the 1905 Tsetserleg (Fig. 9a), 1905 Bolnay (Fig. 9b) and 1950 Mondy (Fig. 9e) earthquakes. This indicates that the historical large earthquakes have significantly impact on the north Hovsgol Fault, which is likely to promote the 2021 Turt earthquake. Given the average stress drop of about 0.72 MPa in the 2021 rupture zone and assuming recurrence earthquakes releasing the same tectonic stress, we suggest that the surrounding historical large events advanced the 2021 earthquake by about 12% recurrence interval. However, the large historical earthquakes have generally stress shadow effect with maximum -0.05 MPa on the south Hovsgol Fault (Fig. 9a), which is attributed to the much larger stress shadow effect caused especially by the 1905

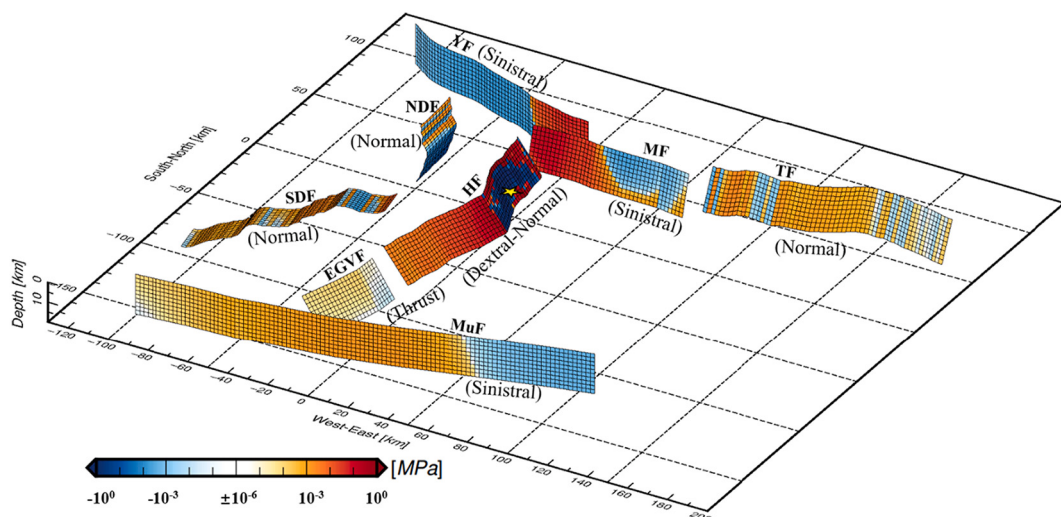


Fig. 8. Distribution of the static ΔCFS in the adjacent active faults induced by the 2021 Turt earthquake. The fault abbreviations are identical to those in Fig. 1b. Yellow star represents the USGS hypocenter. The geometries of the receiver faults labeled by specific fault mechanisms are determined based on the results of this study and information of regional moment tensor and GEM Global Active Faults (Table S4). (For interpretation of the references to colour in this figure legend, the reader is referred to the web version of this article.)

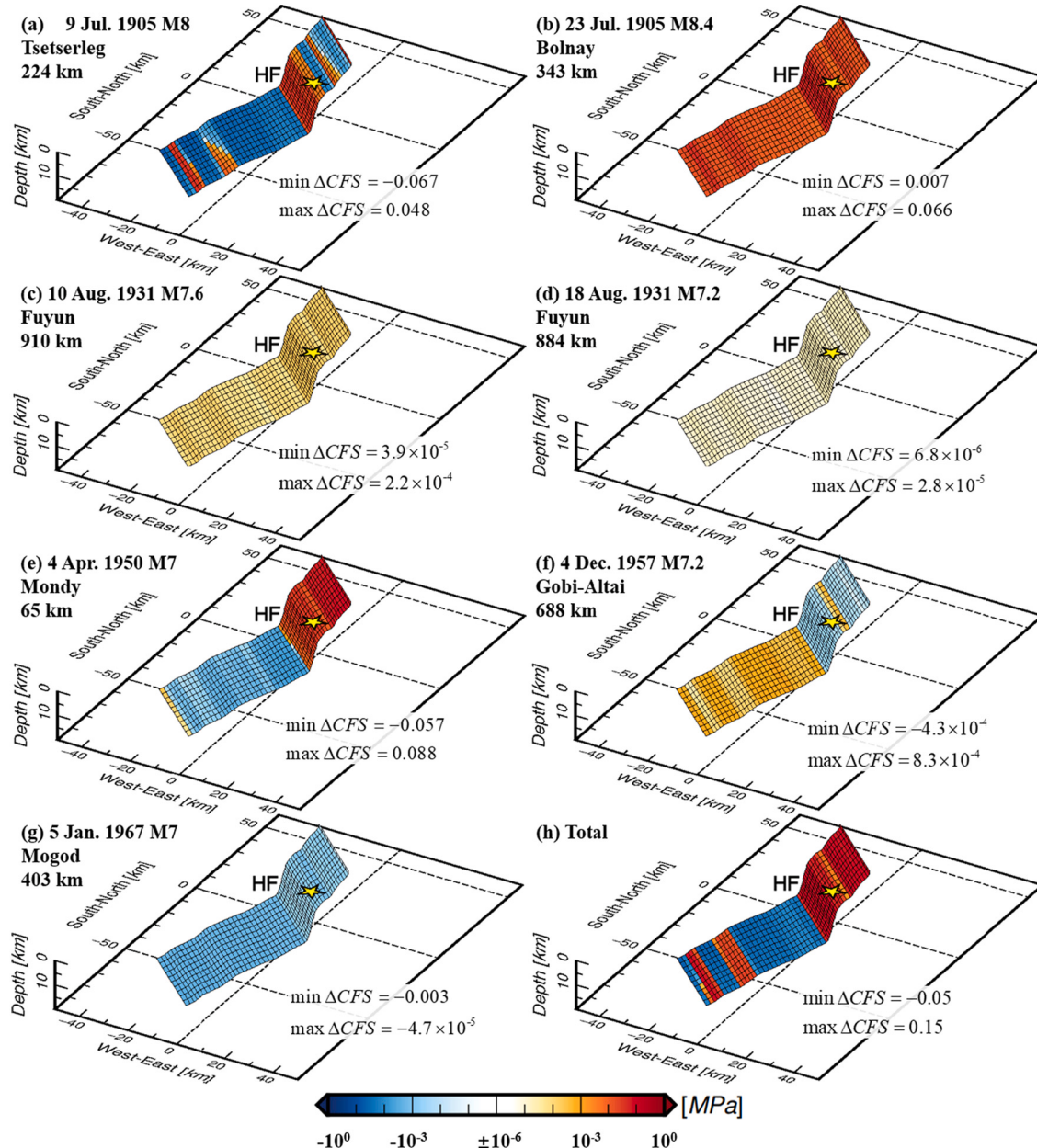


Fig. 9. Distribution of the static ΔCFS on the Hovsgol Fault induced by historical strong earthquakes. (a)-(g) The individual ΔCFS on Hovsgol Fault induced by each strong historical earthquake. Each sub-panel is annotated with the onset time, magnitude, name and distance to the 2021 Turt earthquake of each historical earthquake. (h) The accumulated ΔCFS on Hovsgol Fault caused by the total historical strong earthquakes. The effective friction coefficient is 0.4. Yellow star represents the hypocenter of 2021 Turt earthquake. (For interpretation of the references to colour in this figure legend, the reader is referred to the web version of this article.)

Tsetserleg (-0.067 MPa) and 1950 Mondy (-0.057 MPa) earthquakes than the small stress triggers effect from other events (Fig. 9). This inhibits earthquakes nucleation and can explain why a seismic gap observed on south Hovsgol Fault (Fig. 1b). However, rather strong positive (~ 0.5 MPa, Fig. 8 and Table S4) are observed on the south Hovsgol Fault induced by the 2021 Turt earthquake, which is much large (~ 10 times) than the generally negative (maximum -0.05 MPa) induced by historical large earthquakes (M7, Fig. 1 and 9h). Thus, we suggest that the 2021 Turt earthquake will increase the potential seismic hazard on south Hovsgol Fault, although the south Hovsgol Fault is a seismic gap during the instrumental era.

5. Conclusions

In this study, we investigated the seismogenic fault geometry, coseismic fault slip with surface displacement fields for the Mw6.7 2021 Turt earthquake by using InSAR and teleseismic data. We found that the observations can be best explained by the fault slip on a seismogenic fault with a strike of 341° and a dip angle of 54° . Coseismic slip is characterized by normal faulting with a dextral strike-slip component with a peak value of 1.2 m at 7 km depth. According to InSAR data, up to ~ 20 cm surface subsidence occurred at the hanging wall of the fault. The stress inversion results show that this earthquake occurred within an extensional stress regime with a significant strike-slip component. It is a local area with such a regime being surrounded by transpressive and strike-slip stress fields. This stress heterogeneity is probably controlled

by the distinct structure geometries in and around Hovsgol basin.

The dominated west bank InSAR subsidence and remarkable difference of lithology, seismic activity, lake bottom slope, geomorphology fault scarps, indicate that the current Hovsgol basin is still dominated by half-graben. The calculated ΔCFS induced by the 2021 Turt earthquake suggests the potential seismic hazard associated with the West Mondy Fault and South Hovsgol Fault that deserves further attention. In addition, the ΔCFS caused by the seven historical large earthquakes (M 7) may advance the 2021 Turt earthquake by $\sim 12\%$ recurrence interval. The findings reported here have important implications for regional heterogenous stress field of the crust, graben deformation mechanisms and seismic potential.

Credit author statement

X.L. and W.X. designed the study, organized experimental work. X.L. wrote the original manuscript. X.L. and N.F. conducted the experimental work. X.L., W.X. and N.A.R. led the writing of the manuscript with contributions from all coauthors. All authors commented on, reviewed, and edited the presented version of manuscript.

Declaration of Competing Interest

The authors declare that they have no known competing financial interests or personal relationships that could have appeared to influence the work reported in this paper.

Acknowledgement

We are deeply indebted to Editor Ling Chen and associated editor, three anonymous reviewers for their constructive reviews and comments. We would also like to extend our sincere thanks to Ulziibat Munkhhuu, Zhengyang Pan, Xiaohui Hu and Zhenyue Li for their suggestions and communications during the development of this work. This work was supported by the National Natural Science Foundation of China (No. 42174023). Raw Sentinel-1A data are available from <https://scihub.copernicus.eu/dhus/#/home>. Seismic data are accessed from IRIS (<https://ds.iris.edu>). The aftershocks are from <http://seis-bykl.ru/> and <https://earthquake.usgs.gov/earthquakes/search/>. The processed data used in the study are available (<https://doi.org/10.5281/zenodo.5078988>). The GAMMA commercial software is obtained from <https://www.gamma-rs.ch/software>. The BEAT software is obtained from <https://github.com/hvasbath/beat>. The iterative joint stress inversion software is obtained from <https://www.ig.cas.cz/en/stress-inverse/>. The Coulomb3 software is available from <https://www.usgs.gov/software/coulomb-3>. The Generic Mapping Tools (Wessel et al., 2013) created figures are obtained from <https://www.generic-mapping-tools.org/>.

Appendix A. Supplementary data

Supplementary data to this article can be found online at <https://doi.org/10.1016/j.tecto.2022.229407>.

References

- Arjannikova, A., Larroque, C., Ritz, J.F., Déverchère, J., Stéphan, J., Arjannikov, S., San'kov, V., 2004. Geometry and kinematics of recent deformation in the Mondy-Tunka area (south-westernmost Baikal rift zone, Mongolia-Siberia). *Terra Nova* 16, 265–272. <https://doi.org/10.1111/j.1365-3121.2004.00565.x>.
- Barbot, S., Fialko, Y., Sandwell, D., 2009. Three-dimensional models of elastostatic deformation in heterogeneous media, with applications to the Eastern California Shear Zone. *Geophys. J. Int.* 179, 500–520. <https://doi.org/10.1111/j.1365-246X.2009.04194.x>.
- Bayarraa, J., Ganzorig, D., Wang, K., Bayasgalan, A., Battogtokh, D., 2021. The 2021 Mw 6.7 Khankh earthquake in the Khuvsgul rift, Mongolia. *Mongolian Geoscientist* 26, 46–61. <https://doi.org/10.5564/mgs.v26i52.1361>.
- Bayasgalan, A., Jackson, J., McKenzie, D., 2005. Lithosphere rheology and active tectonics in Mongolia: relations between earthquake source parameters, gravity and GPS measurements. *Geophys. J. Int.* 163, 1151–1179. <https://doi.org/10.1111/j.1365-246X.2005.02764.x>.
- Calais, E., Vergnolle, M., San'kov, V., Lukhnev, A., Miroshnichenko, A., Amarjargal, S., Déverchère, J., 2003. GPS measurements of crustal deformation in the Baikal-Mongolia area (1994–2002): Implications for current kinematics of Asia. *J. Geophys. Res. Solid Earth* 108. <https://doi.org/10.1029/2002jb002373>.
- Chen, C.W., Zebker, H.A., 2001. Two-dimensional phase unwrapping with use of statistical models for cost functions in nonlinear optimization. *J. Opt. Soc. Am. A Opt. Image Sci. Vis.* 18, 338–351. <https://doi.org/10.1364/josaa.18.000338>.
- Del Moral, P., Doucet, A., Jasra, A., 2006. Sequential monte carlo samplers. *J. Royal Statist. Soc.: Series B (Statistical Methodology)* 68, 411–436. <https://doi.org/10.1111/j.1467-9868.2006.00553.x>.
- Delouis, B., Déverchère, J., Melnikova, V., Radziminovitch, N., Loncke, L., Larroque, C., Ritz, J., San'kov, V., 2002. A reappraisal of the 1950 (Mw 6.9) Mondy earthquake, Siberia, and its relationship to the strain pattern at the south-western end of the Baikal rift zone. *Terra Nova* 14, 491–500. <https://doi.org/10.1046/j.1365-3121.2002.00445.x>.
- Dugarmaa, T., Schlupp, A., Adija, M., Ankhtsetseg, D., Bayar, G., Munkhhuu, D., Selenge, L., Tsembe, B., Ulzibat, M., Odonbaatar, C., 2002. *Seismic Map of Mongolia and Site Effect Microzoning at the Capital, Ulaanbaatar*, AGU Fall Meeting Abstracts. S71B-1100.
- Farr, T.G., Rosen, P.A., Caro, E., Crippen, R., Duren, R., Hensley, S., Kobrick, M., Paller, M., Rodriguez, E., Roth, L., Seal, D., Shaffer, S., Shimada, J., Umland, J., Werner, M., Oskin, M., Burbank, D., Alsdorf, D., 2007. The shuttle Radar Topography Mission. *Rev. Geophys.* 45 <https://doi.org/10.1029/2005rg000183>.
- Fialko, Y., Sandwell, D., Simons, M., Rosen, P., 2005. Three-dimensional deformation caused by the 2003 Bam, Iran, earthquake and the origin of shallow slip deficit. *Nature* 435, 295–299. <https://doi.org/10.1038/nature03425>.
- Gephart, J.W., Forsyth, D.W., 1984. An improved method for determining the regional stress tensor using earthquake focal mechanism data: application to the San Fernando earthquake sequence. *J. Geophys. Res. Solid Earth* 89, 9305–9320. <https://doi.org/10.1029/JB089iB11p09305>.
- Gladkochub, D., Donskaya, T., 2009. *Overview of geology and tectonic evolution of the Baikal-Tuva area, Biosilica in Evolution, Morphogenesis, and Nanobiotechnology*. Springer 3–26.
- Hardebeck, J.L., Nazareth, J.J., Hauksson, E., 1998. The static stress change triggering model: Constraints from two southern California aftershock sequences. *J. Geophys. Res. Solid Earth* 103, 24427–24437. <https://doi.org/10.1029/98JB00573>.
- Harris, R.A., 1998. Introduction to special section: stress Triggers, stress Shadows, and Implications for Seismic Hazard. *J. Geophys. Res. Solid Earth* 103, 24347–24358. <https://doi.org/10.1029/98jb01576>.
- Hu, J.-C., Angelier, J., 2004. Stress permutations: Three-dimensional distinct element analysis accounts for a common phenomenon in brittle tectonics. *J. Geophys. Res. Solid Earth* 109. <https://doi.org/10.1029/2003jb002616>.
- Ivanov, A.V., Demeterova, E.I., He, H., Perepelov, A.B., Travin, A.V., Lebedev, V.A., 2015. Volcanism in the Baikal rift: 40 years of active-versus-passive model discussion. *Earth Sci. Rev.* 148, 18–43. <https://doi.org/10.1016/j.earscirev.2015.05.011>.
- Jolivet, M., Arzhannikov, S., Chauvet, A., Arzhannikova, A., Vassallo, R., Kulagina, N., Akulova, V., 2013. Accommodating large-scale intracontinental extension and compression in a single stress-field: a key example from the Baikal Rift System. *Gondwana Res.* 24, 918–935. <https://doi.org/10.1016/j.gr.2012.07.017>.
- Jónsson, S., Zebker, H., Segall, P., Amelung, F., 2002. Fault slip distribution of the 1999 Mw 7.1 Hector Mine, California, earthquake, estimated from satellite radar and GPS measurements. *Bull. Seismol. Soc. Am.* 92, 1377–1389. <https://doi.org/10.1785/0120000922>.
- Khilko, S., Kurushin, R., Kochetkov, V., Misharina, L., Melnikova, V., Gileva, N., Lastochkin, S., Baljinnyam, I., Monkho, D., 1985. *Earthquakes and foundations of seismic zoning in Mongolia. Nauka 222* (in Russian).
- King, G.C., Stein, R.S., Lin, J., 1994. Static stress changes and the triggering of earthquakes. *Bull. Seismol. Soc. Am.* 84, 935–953. <https://doi.org/10.1785/BSSA0840030935>.
- Laske, G., Masters, G., Ma, Z., Pasyanos, M., 2013. Update on CRUST1. 0—A 1-degree global model of Earth's CRUST. *Geophys. Res. Abstr.* 2658.
- Li, Z.W., Ding, X.L., Huang, C., Zhu, J.J., Chen, Y.L., 2008. Improved filtering parameter determination for the Goldstein radar interferogram filter. *ISPRS J. Photogramm. Remote Sens.* 63, 621–634. <https://doi.org/10.1016/j.isprsjprs.2008.03.001>.
- Lin, J., Stein, R.S., 2004. Stress triggering in thrust and subduction earthquakes and stress interaction between the southern San Andreas and nearby thrust and strike-slip faults. *J. Geophys. Res. Solid Earth* 109. <https://doi.org/10.1029/2003JB002607>.
- Liu, X., Xu, W., 2019. Logarithmic Model Joint Inversion Method for Coseismic and Postseismic Slip: Application to the 2017 Mw 7.3 Sarpol Zahab Earthquake. *Iran. Journal of Geophysical Research: Solid Earth* 124, 12034–12052. <https://doi.org/10.1029/2019jb017953>.
- Liu, G., Qiao, X., Yu, P., Zhou, Y., Zhao, B., Xiong, W., 2021. Rupture Kinematics of the 11 January 2021 Mw 6.7 Hovsgol, Mongolia, earthquake and Implications in the Western Baikal Rift Zone. *Seismol. Res. Lett.* 92, 3318–3326. <https://doi.org/10.1785/0220210061>.
- Lu, L., Zhou, Y., 2021. Co- and post-seismic slip analysis of the 2017 MW7.3 Sarpol Zahab earthquake using Sentinel-1 data. *Geodesy and Geodyn.* <https://doi.org/10.1016/j.jgeod.2021.10.004>.
- Lund, B., Slunga, R., 1999. Stress tensor inversion using detailed microearthquake information and stability constraints: Application to Ölfus in Southwest Iceland. *J. Geophys. Res. Solid Earth* 104, 14947–14964. <https://doi.org/10.1029/1999JB900111>.

- Lund, B., Townend, J., 2007. Calculating horizontal stress orientations with full or partial knowledge of the tectonic stress tensor. *Geophys. J. Int.* 170, 1328–1335. <https://doi.org/10.1111/j.1365-246X.2007.03468.x>.
- Martínez-Garzón, P., Ben-Zion, Y., Abolfathian, N., Kwiatek, G., Bohnhoff, M., 2016. A refined methodology for stress inversions of earthquake focal mechanisms. *J. Geophys. Res. Solid Earth* 121, 8666–8687. <https://doi.org/10.1002/2016jb013493>.
- McNamara, D.D., Massiot, C., Lewis, B., Wallis, I.C., 2015. Heterogeneity of structure and stress in the Rotokawa Geothermal Field, New Zealand. *J. Geophys. Res. Solid Earth* 120, 1243–1262. <https://doi.org/10.1002/2014jb011480>.
- Melnikova, V.I., Radzimovich, N.A., Ayyaa, M., 2004. Mechanisms of Earthquake Foci and Seismotectonic Deformations of the Mongolia Region. Complex Geophysical and Seismological Investigations in Mongolia. Research Centre of Astronomy and Geophysics of the Mongolian Academy of Sciences, Ulaanbaatar, pp. 165–170.
- Meltzer, A., Stachnik, J.C., Sodnomambuu, D., Munkhuu, U., Tsagaan, B., Dashdondog, M., Russo, R., 2019. The Central Mongolia Seismic Experiment: Multiple applications of Temporary Broadband Seismic Arrays. *Seismol. Res. Lett.* 90, 1364–1376. <https://doi.org/10.1785/0220180360>.
- Michael, A.J., 1984. Determination of stress from slip data: Faults and folds. *J. Geophys. Res. Solid Earth* 89, 11517–11526. <https://doi.org/10.1029/JB089iB13p11517>.
- Michael, A.J., 1987. Use of focal mechanisms to determine stress: a control study. *J. Geophys. Res.* 92, 357–368. <https://doi.org/10.1029/JB092iB01p00357>.
- Michael, A.J., 1991. Spatial variations in stress within the 1987 Whittier Narrows, California, aftershock sequence: New techniques and results. *J. Geophys. Res. Solid Earth* 96, 6303–6319. <https://doi.org/10.1029/91jb00195>.
- Misharina, L.A., Melnikova, V.I., Baljinnyam, I., 1983. South-western boundary of the Baikal rift zone from the data on earthquake focal mechanism. *Vulkanol. Seismol.* 2, 74–83.
- Nicol, A., Walsh, J., Berryman, K., Nodder, S., 2005. Growth of a normal fault by the accumulation of slip over millions of years. *J. Struct. Geol.* 27, 327–342. <https://doi.org/10.1016/j.jsg.2004.09.002>.
- Pan, Z., He, J., Shao, Z., 2020. Spatial variation in the present-day stress field and tectonic regime of Northeast Tibet from moment tensor solutions of local earthquake data. *Geophys. J. Int.* 221, 478–491. <https://doi.org/10.1093/gji/ggaa013>.
- Petit, C., Déverchère, J., 2006. Structure and evolution of the Baikal rift: a synthesis. *Geochem. Geophys. Geosyst.* 7 <https://doi.org/10.1029/2006gc001265>.
- Petit, C., Déverchère, J., Houdry, F., San'kov, V.A., Melnikova, V.I., Delvaux, D., 1996. Present-day stress field changes along the Baikal rift and tectonic implications. *Tectonics* 15, 1171–1191. <https://doi.org/10.1029/96tc00624>.
- Petit, C., Déverchère, J., Calais, E., Sankov, V., Fairhead, D., 2002. Deep structure and mechanical behavior of the lithosphere in the Hangai-Hövsgöl region, Mongolia: new constraints from gravity modeling. *Earth Planet. Sci. Lett.* 197, 133–149. [https://doi.org/10.1016/S0012-821X\(02\)00470-3](https://doi.org/10.1016/S0012-821X(02)00470-3).
- Pollitz, F., Vergnolle, M., Calais, E., 2003. Fault interaction and stress triggering of twentieth century earthquakes in Mongolia. *J. Geophys. Res. Solid Earth* 108. <https://doi.org/10.1029/2002jb002375>.
- Radzimovich, N.A., Bayar, G., Miroshnichenko, A.I., Demberel, S., Ulzibat, M., Ganzorig, D., Lukhnev, A.V., 2016. Focal Mechanisms of Earthquakes and stress Field of the Crust in Mongolia and its Surroundings. *Geodynam. & Tectonophys.* 7, 23–38. <https://doi.org/10.5800/gt-2016-7-1-0195>.
- Ritz, J., Larroque, C., Stephan, J., Sankov, V., Arjannikova, A., Calais, E., Deverchère, J., Loncke, L., 2000. When compression meets extension: Interaction or competition? The example of the Tunka basin (Western Baikal, Siberia). In: *Proceedings of the Geosciences*, p. 122.
- Ritz, J.F., Arzhannikova, A., Vassallo, R., Arzhannikov, S., Larroque, C., Michelot, J.L., Massault, M., 2018. Characterizing the Present-day activity of the Tunka and Sayan Faults within their Relay Zone (Western Baikal Rift System, Russia). *Tectonics* 37, 1376–1392. <https://doi.org/10.1002/2017tc004691>.
- San'kov, V.A., Miroshnichenko, A.I., Parfeyevets, A.V., Arzhannikova, A.V., Lukhnev, A.V., 2004. Late Cenozoic state of stress in the Earth's crust of the Khubsugul region (Northern Mongolia): Field and experimental evidence. *Geotectonics* 38, 142–152.
- San'kov, V.A., Parfeyevets, A.V., Lukhnev, A.V., Miroshnichenko, A.I., Ashurkov, S.V., 2011. Late Cenozoic geodynamics and mechanical coupling of crustal and upper mantle deformations in the Mongolia-Siberia mobile area. *Geotectonics* 45, 378–393. <https://doi.org/10.1134/s0016852111050049>.
- Schlupp, A., Cisternas, A., 2007. Source history of the 1905 great Mongolian earthquakes (Tsetselerleg, Bolnay). *Geophys. J. Int.* 169, 1115–1131. <https://doi.org/10.1111/j.1365-246X.2007.03323.x>.
- Stein, R.S., King, G.C., Lin, J., 1994. Stress triggering of the 1994 M = 6.7 Northridge, California, earthquake by its predecessors. *Science* 265, 1432–1435. <https://doi.org/10.1126/science.265.5177.1432>.
- Tang, H., Sun, W., 2021. Progress and prospect of deformation theory in the viscoelastic earth. *Rev. Geophys. and Planetary Phys. (in Chinese)* 52, 11–26. <https://doi.org/10.19975/j.dqyx.2020-005>.
- Tapponnier, P., Molnar, P., 1979. Active faulting and cenozoic tectonics of the Tien Shan, Mongolia, and Baykal Regions. *J. Geophys. Res. Solid Earth* 84, 3425–3459. <https://doi.org/10.1029/JB084iB07p03425>.
- Toda, S., Stein, R.S., Richards-Dinger, K., Bozkurt, S.B., 2005. Forecasting the evolution of seismicity in southern California: Animations built on earthquake stress transfer. *J. Geophys. Res. Solid Earth* 110. <https://doi.org/10.1029/2004JB003415>.
- Vasiliev, E.P., Belichenko, V.G., Reznitskii, L.Z., 1997. Relationship between Ancient and Cenozoic structures at the Southwestern flank of the Baikal rift zone. *Doklady Akademii Nauk* 353, 789–792.
- Vasyura-Bathke, H., Dettmer, J., Steinberg, A., Heimann, S., Isken, M.P., Zielke, O., Mai, P.M., Sudhaus, H., Jónsson, S., 2020. The Bayesian Earthquake Analysis Tool. *Seismol. Res. Lett.* 91, 1003–1018. <https://doi.org/10.1785/0220190075>.
- Vavryčuk, V., 2014. Iterative joint inversion for stress and fault orientations from focal mechanisms. *Geophys. J. Int.* 199, 69–77. <https://doi.org/10.1093/gji/ggu224>.
- Vavryčuk, V., Bouchala, F., Fischer, T., 2013. High-resolution fault image from accurate locations and focal mechanisms of the 2008 swarm earthquakes in West Bohemia, Czech Republic. *Tectonophysics* 590, 189–195. <https://doi.org/10.1016/j.tecto.2013.01.025>.
- Vergnolle, M., Pollitz, F., Calais, E., 2003. Constraints on the viscosity of the continental crust and mantle from GPS measurements and postseismic deformation models in western Mongolia. *J. Geophys. Res. Solid Earth* 108. <https://doi.org/10.1029/2002jb002374>.
- Wald, D.J., Heaton, T.H., Hudnut, K.W., 1996. The slip history of the 1994 Northridge, California, earthquake determined from strong-motion, teleseismic, GPS, and leveling data. *Bull. Seismol. Soc. Am.* 86, S49–S70. <https://doi.org/10.1785/BSSA086i01B0S49>.
- Wang, M., Shen, Z.K., 2020. Present-Day Crustal Deformation of Continental China Derived from GPS and its Tectonic Implications. *J. Geophys. Res. Solid Earth* 125. <https://doi.org/10.1029/2019jb018774>.
- Wang, S., Pei, S., Xu, G., Gao, A., 2013. Pn velocity structure at the uppermost mantle of Mongolia and neighboring regions. *Chin. J. Geophys.* 56, 4106–4112. <https://doi.org/10.6038/cjg20131215>.
- Warren-Smith, E., Fry, B., Wallace, L., Chon, E., Henrys, S., Sheehan, A., Mochizuki, K., Schwartz, S., Webb, S., Lebedev, S., 2019. Episodic stress and fluid pressure cycling in subducting oceanic crust during slow slip. *Nat. Geosci.* 12, 475–481. <https://doi.org/10.1038/s41561-019-0367-x>.
- Wegmüller, U., Werner, C., Strozzi, T., Wiesmann, A., Frey, O., Santoro, M., 2016. Sentinel-1 support in the GAMMA Software. *Procedia Comp. Sci.* 100, 1305–1312. <https://doi.org/10.1016/j.procs.2016.09.246>.
- Wessel, P., Smith, W.H.F., Scharroo, R., Luis, J., Wobbe, F., 2013. Generic Mapping Tools: improved Version Released. *EOS Trans. Am. Geophys. Union* 94, 409–410. <https://doi.org/10.1029/2013eo450001>.
- Wileveau, Y., Cornet, F., Desroches, J., Blumling, P., 2007. Complete in situ stress determination in an argillite sedimentary formation. *Physics and Chemistry of the Earth, Parts A/B/C* 32, 866–878. <https://doi.org/10.1016/j.pce.2006.03.018>.
- Wilson, P., Hodgetts, D., Rarity, F., Gawthorpe, R.L., Sharp, I.R., 2009. Structural geology and 4D evolution of a half-graben: New digital outcrop modelling techniques applied to the Nukhul half-graben, Suez rift, Egypt. *J. Struct. Geol.* 31, 328–345. <https://doi.org/10.1016/j.jsg.2008.11.013>.
- Xu, W., 2017. Finite-fault slip model of the 2016 Mw 7.5 Chiloé earthquake, southern Chile, estimated from Sentinel-1 data. *Geophys. Res. Lett.* 44, 4774–4780. <https://doi.org/10.1002/2017gl073560>.
- Xu, W., Rivalta, E., Li, X., 2017. Magmatic architecture within a rift segment: Articulate axial magma storage at Erta Ale volcano, Ethiopia. *Earth Planet. Sci. Lett.* 476, 79–86. <https://doi.org/10.1016/j.epsl.2017.07.051>.
- Xu, G., Xu, C., Wen, Y., Yin, Z., 2019. Coseismic and Postseismic Deformation of the 2016 Mw 6.2 Lampa Earthquake, Southern Peru, Constrained by Interferometric Synthetic Aperture Radar. *J. Geophys. Res. Solid Earth* 124, 4250–4272. <https://doi.org/10.1029/2018jb016572>.
- Yale, D.P., 2003. Fault and stress magnitude controls on variations in the orientation of in situ stress. *Geol. Soc. Lond., Spec. Publ.* 209, 55–64. <https://doi.org/10.1144/GSL.SP.2003.209.01.06>.
- Yang, Y.-H., Tsai, M.-C., Hu, J.-C., Chen, Q., Aurelio, M., Xu, Q., Jiang, Z., Xu, L., Yang, C., Li, L., 2021. Assessment of the Seismic Hazards of the Marikina Valley Fault from 2019 Mw 6.1 Castillejos Earthquake and Historical Events. *Seismol. Res. Lett.* 92, 3360–3374. <https://doi.org/10.1785/0220200373>.
- Zheng, A., Chen, X., Xu, W., 2020. Present-Day Deformation Mechanism of the Northeastern Mina Deflection Revealed by the 2020 Mw 6.5 Monte Cristo Range Earthquake. *Geophys. Res. Lett.* 47. <https://doi.org/10.1029/2020gl090142>.
- Zoback, M.L., 1992. First- and second-order patterns of stress in the lithosphere: the World Stress Map Project. *J. Geophys. Res.* 97, 11703–11728. <https://doi.org/10.1029/92jb00132>.
- Zorin, Y.A., Tumtanov, E.K., Arvisbaatar, N., 1989. Structure of Cenozoic basins of the Prekhubsugul region from gravity data. *Russ. Geol. Geophys.* 10, 130–136.